

## Research Article

# CFD Analysis of the Sideslip Angle Effect around a BWB Type Configuration

Arim Ko,<sup>1</sup> Kyoungsik Chang ,<sup>2</sup> Dong-Jin Sheen,<sup>3</sup> Young-Hee Jo,<sup>4</sup> and Ho Joon Shim<sup>5</sup>

<sup>1</sup>Department of Aeronautical System Engineering, Hanseo University, Republic of Korea

<sup>2</sup>School of Mechanical Engineering, University of Ulsan, Republic of Korea

<sup>3</sup>Department of Aeromechanical Engineering, Hanseo University, Republic of Korea

<sup>4</sup>Agency for Defense Development, Republic of Korea

<sup>5</sup>Department of Unmanned and Autonomous Engineering, Kyungwoon University, Republic of Korea

Correspondence should be addressed to Kyoungsik Chang; [kschang76@ulsan.ac.kr](mailto:kschang76@ulsan.ac.kr)

Received 28 January 2019; Accepted 17 February 2019; Published 23 April 2019

Academic Editor: Angel Velazquez

Copyright © 2019 Arim Ko et al. This is an open access article distributed under the Creative Commons Attribution License, which permits unrestricted use, distribution, and reproduction in any medium, provided the original work is properly cited.

In this study, we conducted numerical simulations for a nonslender BWB type planform with a rounded leading edge and span of 2.0 m to analyze the effect of the sideslip angle on the planform at a freestream velocity of 60 m/s. The Reynolds number based on the mean chord length was  $2.9 \times 10^6$ , and we considered the angle of attack ranging from  $-4^\circ$  to  $16^\circ$  and sideslip angles up to  $20^\circ$ . We used an unstructured mesh with a prism layer for the boundary layer with  $1.11 \times 10^7$  grid points, and the  $k-\omega$  SST turbulence model. We analyzed force and moment coefficients with respect to variation of angle of attack and sideslip angles. Side force and rolling/yawing moment coefficients had highly nonlinear relationships with the sideslip angle while lift and drag coefficients were not significantly affected. We interpreted the mechanism of these aerodynamic characteristics based on pressure and skin friction contours. Suction pressure near the leading edge had a marked effect on the pitching and rolling moment. We identified five flow types on the blunt leading edge swept wing by skin friction lines and off-body streamlines at a high angle of attack and sideslip angles.

## 1. Introduction

There is an advantage of a high lift-to-drag ratio aerodynamically in the BWB (blend wing body) type planform, of which the recent models are the 1303 UCAV (unmanned combat air vehicle) developed by the US AFRL and SACCON (Stability And Control CONfiguration) by NATO RTO AVT-161, than the conventional fixed wing one. This is because the BWB-type planform shows the aerodynamic features of the delta wing with the leading edge vortex. The primary leading edge vortex is generated from the interaction between the separated shear layer at the leading edge and the freestream. The secondary leading edge vortex occurs when the reattached flow is separated again by the adverse pressure gradient in the spanwise direction. The vortex lift is an additional lift provided by the local suction pressure near the leading edge. The nonlinear behavior of the pitching, rolling, and yawing moments is created by movement of the vortex [1].

The behavior of the vortex on this type of planform is sensitive to some parameters such as the swept angle [2, 3], the sharp or rounded leading edge [4, 5], the angle of attack and angle of sideslip, and the Reynolds number. Many experimental [4, 6, 7] and CFD (computational fluid dynamics) studies [5, 8–11] were conducted to understand the flow behavior including the leading edge vortex around the low swept delta wings. The vortical flow around the SACCON configuration was investigated through both wind tunnel experiments and numerical simulation by Schütte et al. [12]. For various angles of attack, the flow was governed by the complicated vortices structures, which led to overall nonlinear aerodynamic behavior. The experimental and numerical results were generally in good agreement with slight differences for the angle of attack ( $16^\circ$ - $18.5^\circ$ ) at which the dip in the pitching moment curve was located as well as for the sharpness of the dip. Petterson [13] applied steady RANS (Reynolds-averaged Navier-Stokes) computations to the

1303 UCAV configuration for the validation of the code and the evaluation of various turbulence models. All adopted turbulence models showed reasonable agreement with experimental lift polar, but poor agreement with drag at low angles of attack. The main characteristics of the pitching moment curve were captured, including  $C_M/\alpha$  gradient, the pitch break angle, and the subsequent sharp nose up. The authors showed that CFD results can be used with confidence in the design and performance evaluation process steps for control sizing and low speed pitch authority during landing and take-off. However, most of the numerical simulations focused on validation and prediction of aerodynamic characteristics including the coefficients of drag, lift, and pitching moment only with respect to changes in the angle of attack. Computational size and cost restrict the range of simulation to the longitudinal properties with zero sideslip; therefore, a few have studied the effect of the sideslip angle on the BWB-type configuration [14, 15].

Loeser et al. [14] conducted the experiment measuring static force and pressure in the SACCON model for various angles of attack ( $-5^\circ$ - $10^\circ$ ) and sideslip angles ( $-10^\circ$ - $10^\circ$ ) in two different wind tunnels: DNW-NWB and NASA LaRC. The measured aerodynamic data in two wind tunnels were compared, and the effect of the leading edge type, Reynolds number, and sling mount support was investigated. Also, the test results provided the CFD researchers with reference data for validation and verification of the used code. Shim et al. [15] investigated the sideslip angle effect in the lambda wing configuration through the subsonic wind tunnel test. They found that the unstable pitch break was delayed to a higher angle of attack as the sideslip angle increased. The yawing moment was shown to be unstable with increased slope as the sideslip angle increased. Frink [16] studied on the aerodynamic stability and control predictive capability of time-accurate RANS methodology for a 53-degree swept UCAV configuration. He considered static longitudinal/lateral sweeps and a specified roll/pitch/yaw sinusoidal dynamic motion. He found the aerodynamic characteristics by the complex nonlinear physics of round leading edge vortex separation with comparison with experimental data. Ghoreyshi and Cummings [17] investigated the reduced order model based on the CFD simulation results to create a full aerodynamics database and proposed the new approach to improve the accuracy of prediction of static and dynamic characteristics of the SACCON UCAV. CFD results showed that the lateral airloads become highly nonlinear with the sideslip angle even at low angles of attack. The unsteady aerodynamic characteristics of the SAGITTA diamond-wing configuration at low speed conditions were investigated by Pfnür and Breitsamter [18]. The nonlinear behavior of the pitch-damping derivative and yaw-damping were observed with respect to the angle of attack and sideslip angle. They concluded that the nonlinearities are associated with occurring flow separation and vortex formation at the blunt leading edge.

Yayla et al. [19] studied the structures of the leading edge vortex over the nonslender diamond wing experimentally. Their experiment focused qualitatively on the flow phenomenon using the dye visualization apparatus, specifically the

vortex breakdown at various sideslips ( $0^\circ$ - $15^\circ$ ). When the sideslip angle increased beyond  $4^\circ$ , vortex breakdown occurred in the downstream region of the diamond wing's trailing edge on the leeward side, but vortex breakdown took place further upstream on the windward side. Recently, the task group AVT-183 within the NATO Science and Technology Organization (STO) focused on the swept blunt leading edge flow separation problem using a  $-53^\circ$  swept diamond wing in a study titled, "Reliable prediction of flow separation onset and progression for air and sea vehicles." This project was initiated to examine in more detail vortical flow structures on the delta wing geometry relevant to the BWB-type planform. Research groups such as NASA, ONERA, and others tried to elucidate the mechanism of incipient separation and subsequent vortex formation with five distinct flow types from the blunt leading edge through numerical simulations with various turbulence models and experiments [20, 21].

In the present study, we conducted numerical simulations on the geometry of the BWB-type planform and compared aerodynamic coefficients with the experimental results by Shim et al. [15]. Specifically, we studied the effects of the sideslip angle through detailed investigation of vortical structures and aerodynamic coefficients including rolling and yawing moment. We also analyzed the incipient separation and subsequent vortex formation using simulation results including skin friction lines, off-body streamlines, and flow variable contours from the perspective of five distinct flows explained by the NATO/STO AVT-183 task group.

## 2. Numerical Methods and Simulation Setup

The geometry in the present study was the same as that in the experiment by Shim et al. [22], and the specifications are shown in Figure 1. This model composed of NACA 64A210 airfoil has a wingspan of 2,000 mm, a body centerline length of 1181.36 mm, and a mean aerodynamic chord (MAC) of 708.3 mm. The swept angle of the leading edge is  $47^\circ$  and the crank angle,  $30^\circ$ . The washout angle ( $\epsilon$ ) was set from  $\eta = z/(b/2) = 0.407$  to  $\eta = 0.860$  linearly and  $-5^\circ$  to the wing tip. This washout was to ensure that at stall speed the wing root had the stall earlier than the wing tip, and the spanwise lift distribution was modified to reduce the lift-induced drag. The moment reference point (MRP) was set to 602 mm from the apex as in the prior experiment [22].

Figure 2 shows the coordinate system used in the present work. CFD simulation uses Cartesian coordinates with  $x$ ,  $y$ , and  $z$  axes as shown in the figure. The angle of attack and sideslip angle were defined as  $\alpha$  and  $\beta$  (degrees) in the given coordinate system. The direction of positive moment is represented by the curved arrow. The pitching and yawing moments have the same direction as the displayed coordinate while the rolling moment is opposite the direction on the  $x$ -axis.

We set the computational domain to box type with length in the streamwise direction of 20C (C is the root chord length) and width in the spanwise direction of 14C. The height in the vertical direction changed linearly from 10C

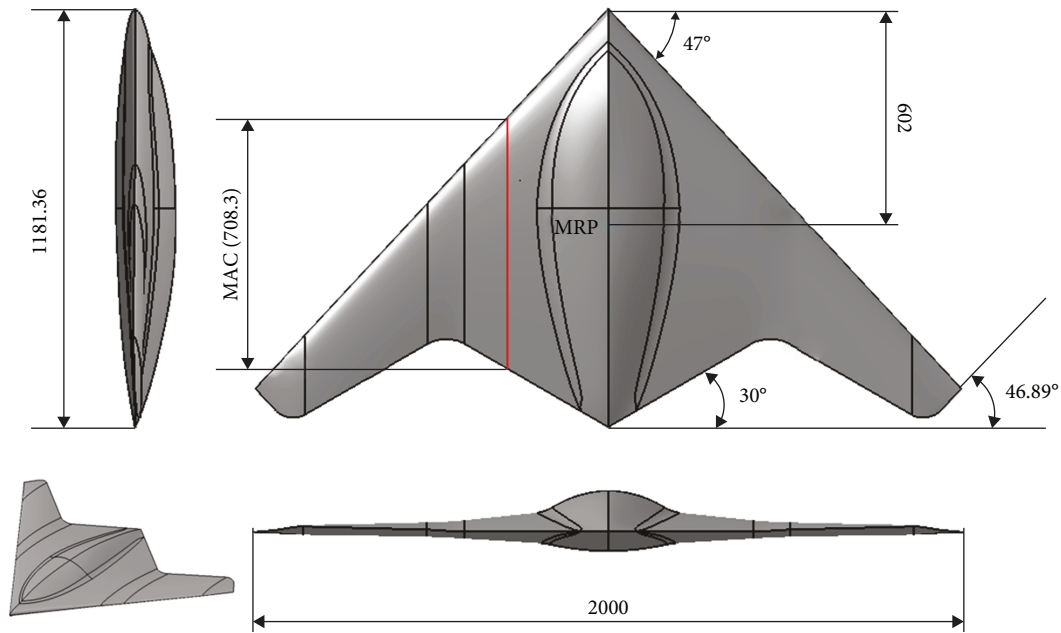


FIGURE 1: BWB-type planform and geometric parameters.

at the inflow boundary to  $24C$  at the outflow boundary. The grid inside the computational domain was generated with commercial software, ICEM-CFD of ANSYS [23]. The density tool in ICEM-CFD was applied to increase the density of the volume mesh near the leading/trailing edge and the wing tip in order to ensure correct simulation of the region with high velocity and pressure gradient. We used the unstructured mesh, and set the prism mesh with an initial height of 0.01 mm and 20 total layers to resolve the turbulent boundary layer. There were  $1.11 \times 10^7$  total grid cells. Figure 3 shows the computational domain and mesh generated around the model. We used the contours of the  $y^+$  distribution over the upper wall of the model at an angle of attack of  $0^\circ$  to ensure that the wall unit  $y^+$  would be about or less than 1.0 in order to resolve the turbulent boundary layer in the  $k - \omega$  SST (shear stress transport) model (Figure 4).

We solved incompressible Navier-Stokes equations with the second-order discretization scheme in space and time and corrected the pressure-velocity using a SIMPLE (Semi-Implicit Method for Pressure-Linked Equation) algorithm. We used the  $k - \omega$  SST turbulent model and discretized two equations with the second order. We used the commercial CFD code, ANSYS Fluent V18.2.

We set the freestream velocity to 60 m/s as in Shim et al. [22]. The Reynolds number based on the mean chord length, and the freestream velocity is  $2.9 \times 10^6$ . We varied the angle of attack from  $0^\circ$  to  $16^\circ$  with a constant interval of  $2^\circ$ . The sideslip angle ranged from  $0^\circ$  to  $8^\circ$ , and extra angles of  $14^\circ$  and  $20^\circ$  were considered. The detailed flow conditions are summarized in Table 1.

### 3. Results

**3.1. Validation.** The grid system and numerical schemes including the turbulence model were validated by comparison

with experimental results by Shim et al. [22]. Figure 5 shows the lift and drag coefficients according to the angle of attack. The lift coefficient was linear up to a  $12^\circ$  angle of attack, and then the slope decreased thereafter. The drag coefficient showed a typical pattern, which was a slow increase at a small angle of attack and rapid divergence at a large one, consistent with findings for other BWB-type planforms such as the 1303 UCAV [13] and SACCON [5]. An overall good agreement was observed in the two aerodynamic coefficients between numerical simulations and experimental data [22]. However, there was overprediction of the drag coefficient between  $10^\circ$  and  $14^\circ$ , and this tendency was also observed in Petterson's simulation results [13]. Figure 6 shows the comparison of the pressure coefficient at four stations ( $\eta = 0.285, 0.4, 0.65,$  and  $0.785$ ) in the spanwise direction at a  $12^\circ$  angle of attack where the separation started and the region of suction pressure decreased from near the wingtip. The suction pressure distribution near the leading edge agreed well with experimental data at all but the last of the inboard stations ( $\eta = 0.785$ ). At the last station, there was a small underprediction in the strength of the leading edge vortex, and the magnitude of the adverse pressure gradient was slightly less than that of the reference. This discrepancy between the simulation and experiment in other numerical simulations of BWB-type planforms was previously reported by Petterson [13].

**3.2. Aerodynamic Coefficients.** Figure 7 shows the lift, drag, and side force coefficients with respect to the angle of attack at various sideslip angles. The sideslip angle had little effect on the lift and drag force coefficients except at a large angle of attack (greater than  $12^\circ$ ) where the change was within 5% when compared with the values at a sideslip angle of zero. However, the side force coefficient was markedly affected by the sideslip angle as expected. There was little variation at a

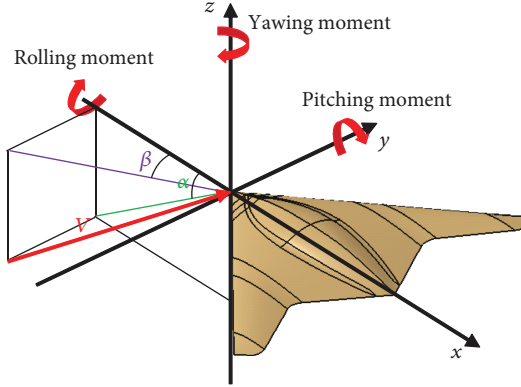


FIGURE 2: Coordinate system and sign convention of moment.

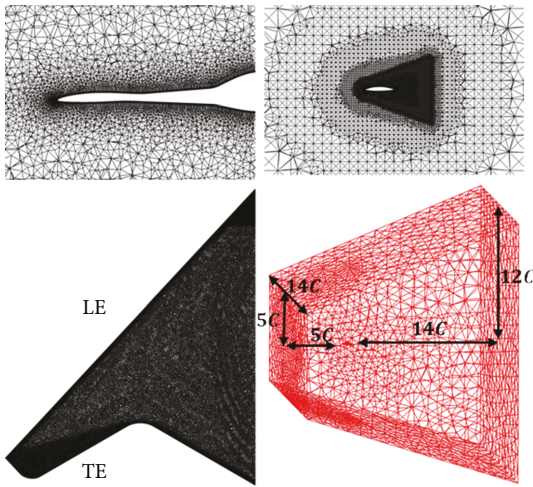


FIGURE 3: Computational domain and grid details.

small angle of attack (up to  $8^\circ$ ). However, there was an abrupt decrease in the coefficient near a  $12^\circ$  or  $14^\circ$  angle of attack with the opposite sign and then there is an increase with the original sign again. The abrupt decrease seems to be related with the asymmetric leading edge vortex between the leading edge in the windward side and leeward side wing. The force component in the  $y$ -direction by the suction pressure at the windward side is dominant that that at opposite side wing, which is shown in Figure 8. This will be discussed in more detail at the next chapter, flow field results. This finding is consistent with Loeser's experiment results [14]. The larger the sideslip angle, the greater the change at the inflection point.

We plotted the coefficients of pitching, rolling, and yawing moments to investigate the effect of sideslip angle in Figure 9. In general, the BWB-type planform showed an unstable behavior with an abrupt increase in the pitching moment coefficient as the angle of attack increased, which is called pitch break. When the sideslip angle was zero, the pitch break started at an  $8^\circ$  angle of attack in the present model. As the sideslip angle increased, the pitch break was delayed up to an angle of attack of  $12^\circ$ . After the pitch break angle of attack, the pitching moment coefficient increases

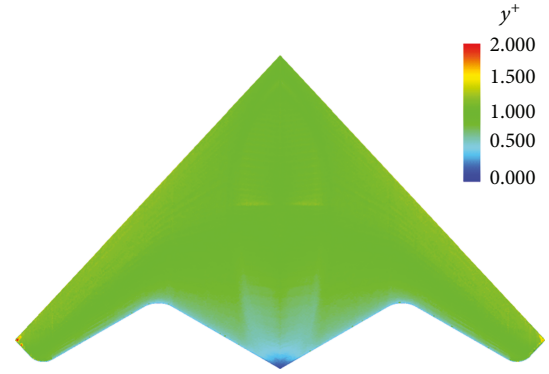
FIGURE 4:  $y^+$  contours of upper surface at zero angle of attack.

TABLE 1: Model and flow parameters.

Conditions	Unit	Present model
Span	mm	2,000
MAC	mm	708.3
Swept angle	$^\circ$	47
Washout	$^\circ$	-5
Freestream velocity	m/s	60
Angle of attack	$^\circ$ (deg)	-4~16 with $\Delta\alpha = 2$
Sideslip angle	$^\circ$ (deg)	0, 2, 4, 6, 8, 14, 20

less at a large sideslip angle than that at a small sideslip angle. For example, when the sideslip angles were 0 and 20, the moment change was  $0.03(=0.01-(-0.02))$  and  $0.01(=-0.015-(-0.025))$ , respectively, between the pitch break starting angle and an angle of attack of  $16^\circ$ . Before the angle of attack where the pitch break happened, there was a slight decrease in the pitching moment coefficient. These tendencies are highly consistent with experimental data reported by Shim et al. [15].

As expected, the rolling and yawing moment coefficients were markedly affected by the sideslip angle. At a sideslip angle of zero, the rolling and yawing moment coefficients were nearly zero, except at large angles of attack ( $16^\circ$  in the rolling moment and  $12^\circ$ - $16^\circ$  in the yawing one). Even though the ideal value of this coefficient at a sideslip angle of zero should be zero, the grid along the symmetric plane (root chord,  $\eta = 0$ ) was not perfectly symmetric and complex flow such as separation bubbles enhanced the asymmetric flow field. This discrepancy can be easily encountered in the unstructured grid system. Similar results showing deviation from zero even in symmetric flow conditions were reported by Loeser et al. [14]. They surmised that asymmetry in the model geometry and effectiveness of the carborundum strip caused this problem.

As the angle of attack increased at a non-zero sideslip angle, the rolling moment coefficient increased until an angle of attack of  $10^\circ$  or  $12^\circ$  and decreased thereafter. The angle of attack with the maximum rolling moment value increased with the sideslip angle. Loeser et al. [14] and Shim et al. [15] observed the same behavior of the rolling moment coefficient as well as a decrease after the maximum angle of attack

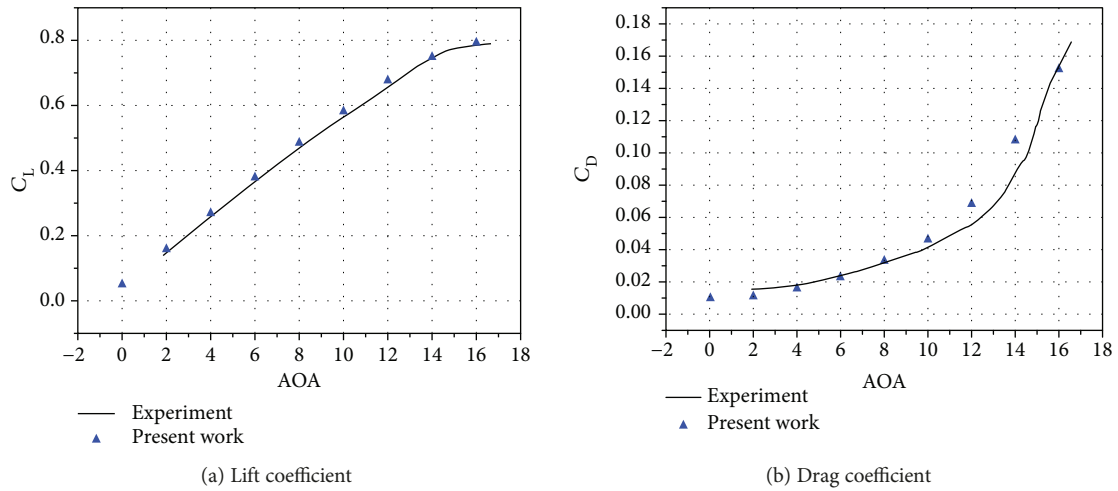


FIGURE 5: Lift and drag coefficients for angle of attack.

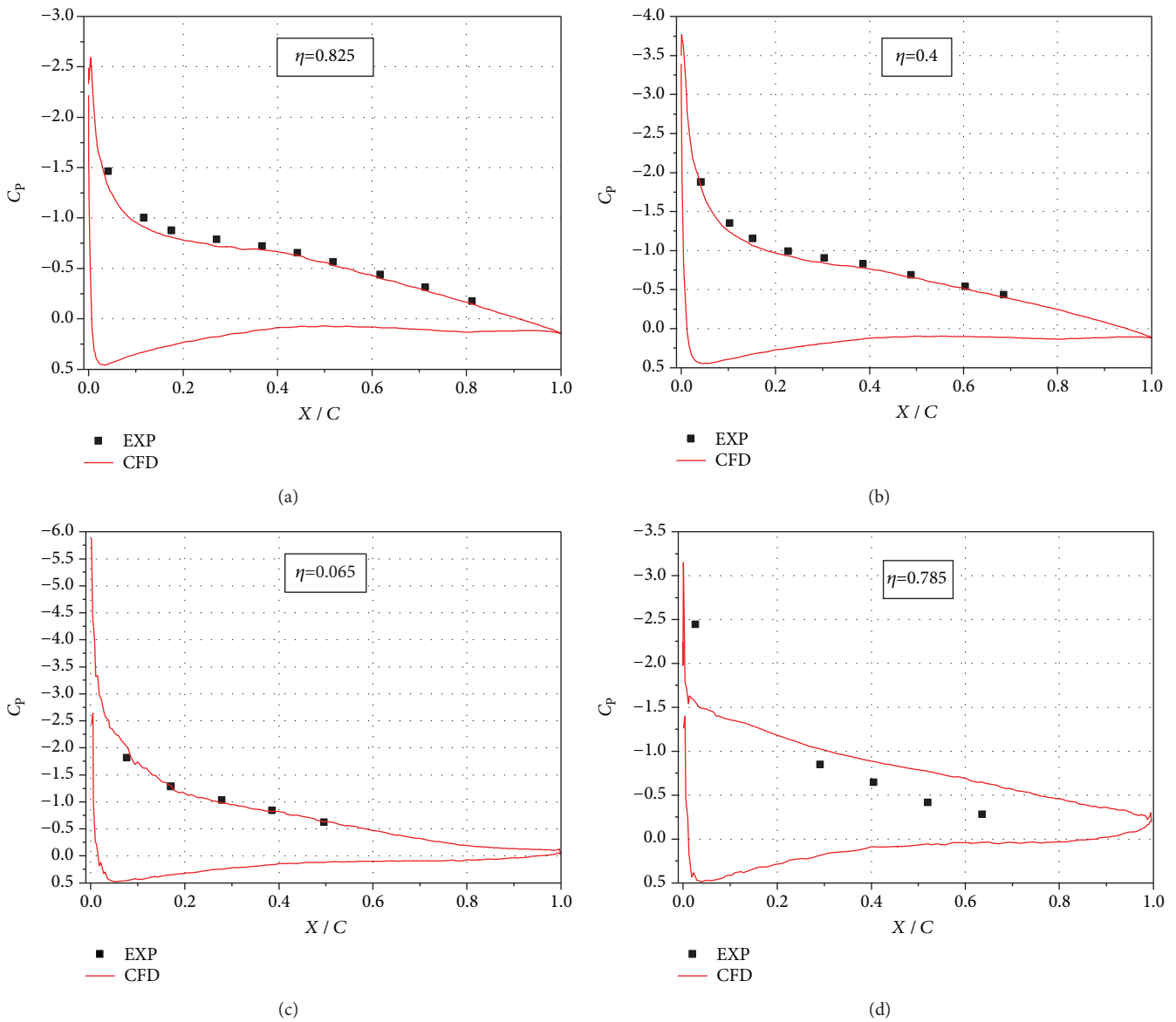


FIGURE 6: Pressure coefficient of four stations ( $\eta = 0.285, 0.4, 0.65, \text{ and } 0.785$ ) at an angle of attack  $12^\circ$ .

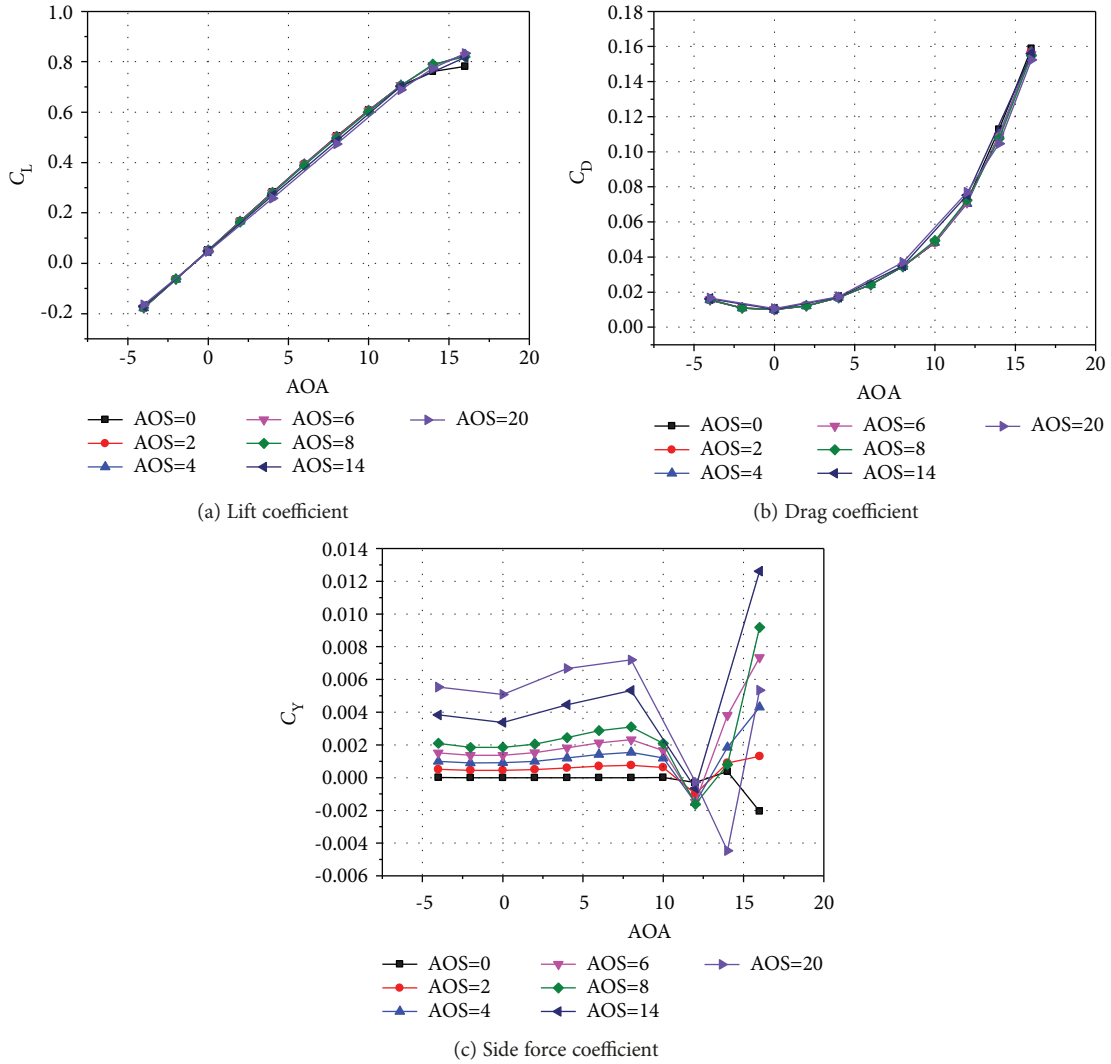


FIGURE 7: Lift, drag, and side force coefficients for angle of attack.

to a negative value, which is beyond the scope of the present work. When the sideslip angle increased, the rolling moment coefficient increased above an angle of attack of 1.5-2.0°, but the coefficient decreased negatively below this angle of attack. This non-zero angle of attack (approximately 1.5-2.0°) where a zero rolling moment occurs is due to the balance between lift and side forces.

The yawing moment coefficient also showed a strong nonlinear behavior with variation in the sideslip angle. Like the rolling moment coefficient, an exactly zero moment could not be obtained due to the asymmetric grid structure and highly separated flow structures. As the angle of attack increased, the yawing moment coefficient showed little change until an angle of attack of 8-10°. However, there was a rapid decrease in the coefficient with a peak and then an abrupt increase. The magnitude of the peak increased with the angle of the sideslip. Similarly with the side force coefficient, the nonlinear characteristics of the yawing moment coefficient occurs near the angle of attack, 12°~14°, which can be inferred from the

asymmetric leading edge vortex between both side wings. The negative yawing moment coefficient means that the balance of the  $y$ -direction force is dominant in the clockwise direction based on the MRP. It can be confirmed that the force component in the  $y$ -direction by the suction pressure near the leading edge is displayed with a larger value downstream the MRP in the windward side than in the leeward side one.

For a more detailed analysis of the sideslip angle effect, we plotted the sideslip force, rolling moment, and yawing moment with respect to the sideslip angle in Figure 10. In Loeser's experiment [14], it is revealed that the side force coefficients differed both in magnitude and in slope at two angles of attack of 15 and 17° with other angles of attack. The same behavior was observed between an angle of attack of 12° and other angles of attack in the present work. This phenomenon can be inferred from the plot of the side force coefficient with respect to the angle of attack in Figure 7(c). At other angles of attack, the coefficient was positive and tended to increase with the sideslip angle.

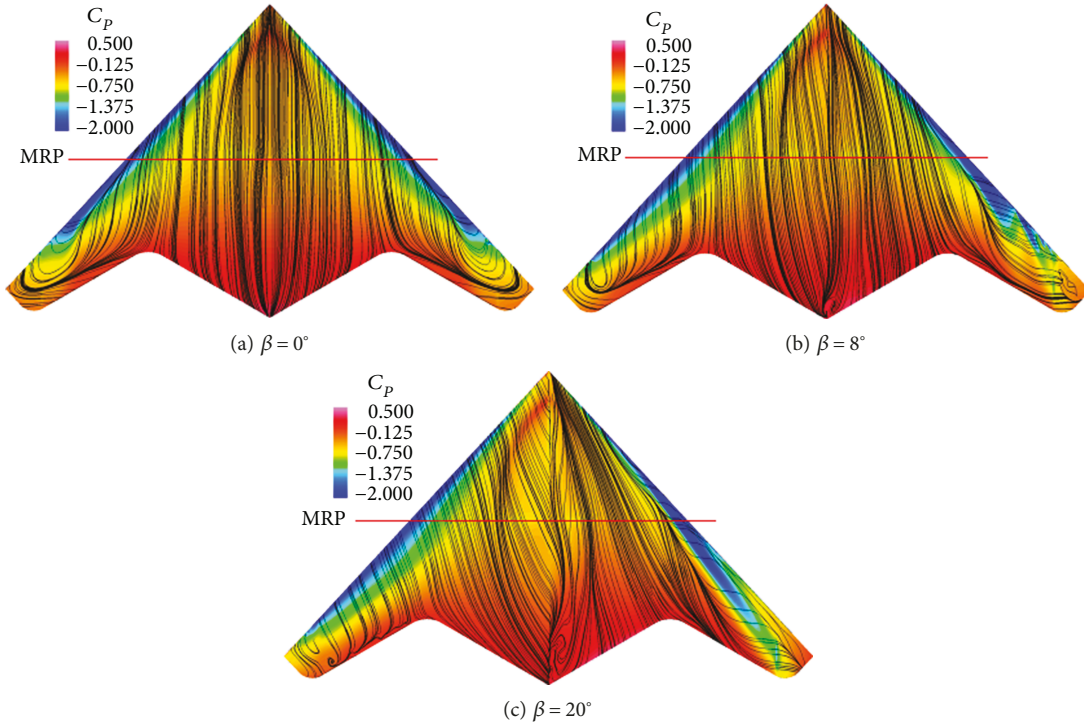


FIGURE 8: Skin friction lines and pressure coefficient contours at angle of attack  $12^\circ$ .

The rolling moment coefficient was positive, and the slope of  $\partial C_{MX}/\partial\beta$  was positive after the critical angle of attack, which was estimated to be  $1.5^\circ$  based on the  $x$ -intercept in Figure 9(b), but the reverse trend occurred before this angle. As mentioned above, the present model adopted the washout,  $5^\circ$  to delay the stall in the wing tip than in the wing root. This washout has an effect on the non-zero angle of attack where the opposite behavior of the rolling moment coefficient happens. The rolling moment coefficient demonstrated a highly nonlinear behavior beginning at an angle of attack of  $16^\circ$ , as evidenced by the different slopes at each sideslip angle. Loeser et al. [14] showed similar results with no change in the sign or gradient of  $\partial C_{MX}/\partial\beta$  below a  $10^\circ$  angle of attack and a highly nonlinear one of the gradient thereafter.

Similarly, the yawing moment coefficients showed a nonlinear behavior after an angle of attack of  $12^\circ$ . At small angles of attack, there was little change with increasing sideslip angle. However, at an angle of attack of  $12^\circ$ , the magnitude of the coefficient and the gradient of  $\partial C_{MZ}/\partial\beta$  increased abruptly, which was the source of increasing lateral motion instability of the planform. As the sideslip was increased, the gradient was changed positively at small sideslip angles ( $\sim 8^\circ$ ) and then became negative again after a sideslip angle of  $14^\circ$ . The values were positive ones, which differed from those at  $14^\circ$ . The same trends were shown by Loeser et al. [14], but these critical angles of attack were  $15^\circ$  and  $17^\circ$ , whereas our results predicted these angles to be  $12^\circ$  and  $16^\circ$  due to the different geometry of the planform.

**3.3. Flow Field Results.** We investigated the highly nonlinear behaviors of the aerodynamic force and moment coefficients

in more detail from a physics perspective by analyzing flow field parameters including contours and streamlines. Figures 8, 11, and 12 show the contours of the pressure coefficient and skin friction line, which we calculated streamline from the wall shear stress at three angles of attack ( $0^\circ$ ,  $12^\circ$ , and  $16^\circ$ ) and three sideslip angles ( $0$ ,  $8$ , and  $20^\circ$ ). We observed symmetric skin friction lines and pressure contours with respect to the wing root at a sideslip angle of zero (Figures 8(a), 11(a), and 12(a)), which is consistent with the simulation results of Park et al. [24] which considered the geometry with half of the body irrespective of the sideslip angle. At an angle of attack  $12^\circ$ , the most region of the leading edge was occupied by suction pressure; however, at an angle of  $16^\circ$ , this region moved to the apex while the remaining parts entered the stall. Consequently, the amount of lift by the leading edge vortex decreased and the pitching moment coefficient exhibited an unstable behavior with a rapid increase in the nose-up direction.

At an angle of attack of zero, as the sideslip angle increased, the rolling moment coefficient decreased linearly with a negative slope at a sideslip angle of zero (Figure 10(b)). Figure 11 shows that as the sideslip angle increased, the pressure near the leading edge of the windward wing (left side of the figure) was higher than that of the leeward (right side of the figure) side, even though the low-pressure region inboard was more prolific on the windward wing than on the leeward one.

On the contrary, two cases in which there was a non-zero angle of attack showed different flow patterns with positive values and slopes of the rolling moment coefficient. Increases in the sideslip angle caused the spanwise velocity component to increase and then the pressure of the lower surface (not

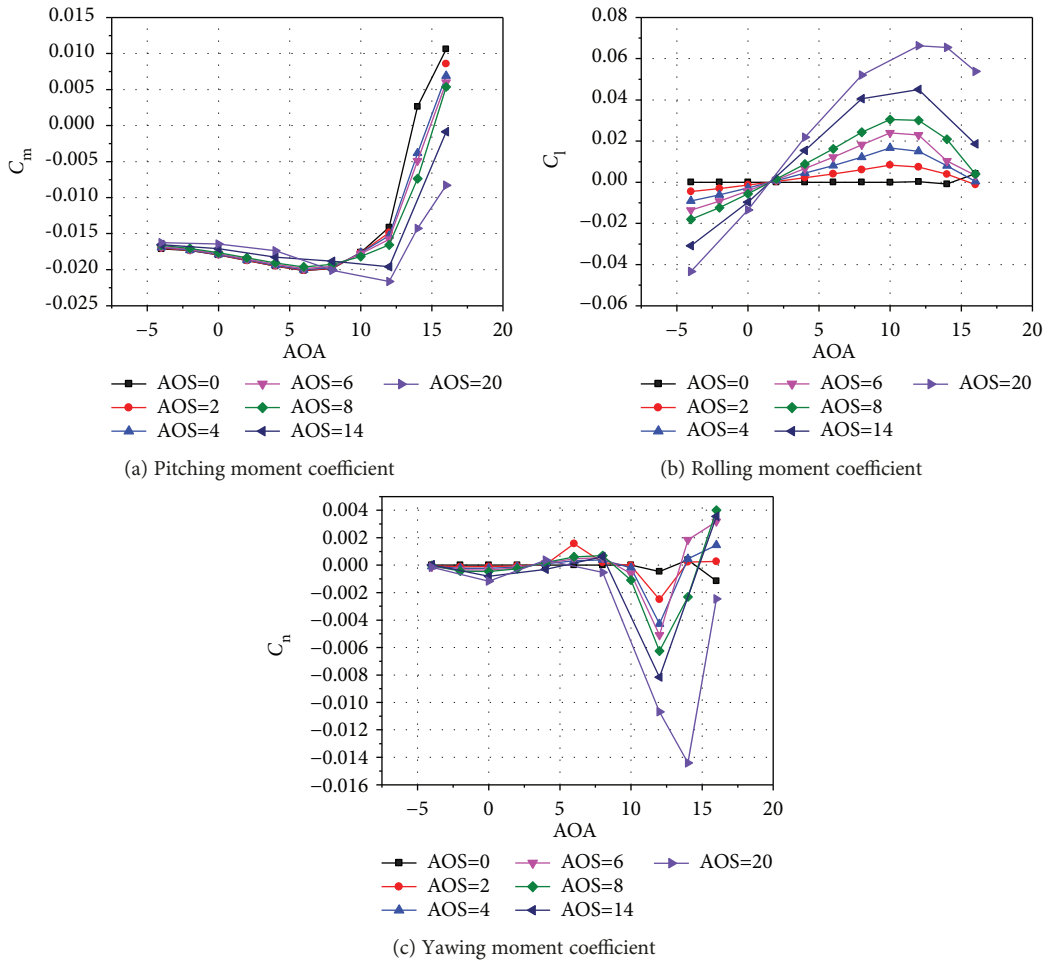


FIGURE 9: Pitching, rolling, and yawing moment coefficient for angle of attack.

shown here) on the windward wing increased into a positive rolling moment. As shown in Figures 8 and 12, the suction pressure region near the leading edge increased with the sideslip angle, but this region on the downstream and leeward sides move inboard, which resulted in an increase in the rolling moment coefficient. Another interesting point is that at a sideslip angle of 8°, the rolling moment coefficient at a 16° angle of attack was less than that at 12° (refer to Figure 10(b)), which means that the coefficient peaked at 10-12° and then decreased after these angles of attack. It seems that the decrease in suction pressure near the leading edge on both wings was less on the leeward wing than on the windward one. We confirmed this by comparing the pressure coefficient contours in Figures 8(b) and 12(b). The same mechanism can be applied to the case where the angles of attack changed from 12° to 16° at a sideslip angle of 20°. The difference in the suction pressure region is demonstrated clearly by comparing Figures 8(c) and 12(c).

Figure 13 shows the skin friction contours with skin friction lines as an analysis of the behavior of the yawing moment coefficient. As the sideslip angle increased at an angle of attack of 12°, the skin friction between the primary attachment line and the secondary separation line increased

on the leeward side wing, which is consistent with the diamond wing simulation results by Frink et al. [20]. The streamwise velocity component also decreased with the sideslip angle, and the component near the outboard far from the momentum reference point had a marked effect on the yawing moment. These factors caused a negative increase in the yawing moment coefficient.

There are five distinct flow types for a blunt leading edge swept wing: (1) the incipient separation that coalesces into (2) the leading edge vortex that induces (3) the secondary vortex separation, which is bracketed by (4) the inner attached flow and (5) an inner vortex separation. Frink et al. [20] analyzed the incipient separation and subsequent vortex formation of 53° swept diamond wing at an angle of attack of 12° based on the simulation results. In the present work, we saw only the primary leading edge vortex and related separation in most cases, and this is related to the medium swept angle (47°) of the present platform. As the sideslip angle increased to 20°, which means that the extra incidence angle in the yawing direction was added to eventually reach 67° on the leeward wing, the secondary vortex, and the inner vortex formed on this part of the wing. Figures 8(c), 11(c), and 12(c) show three different angles of attack with a

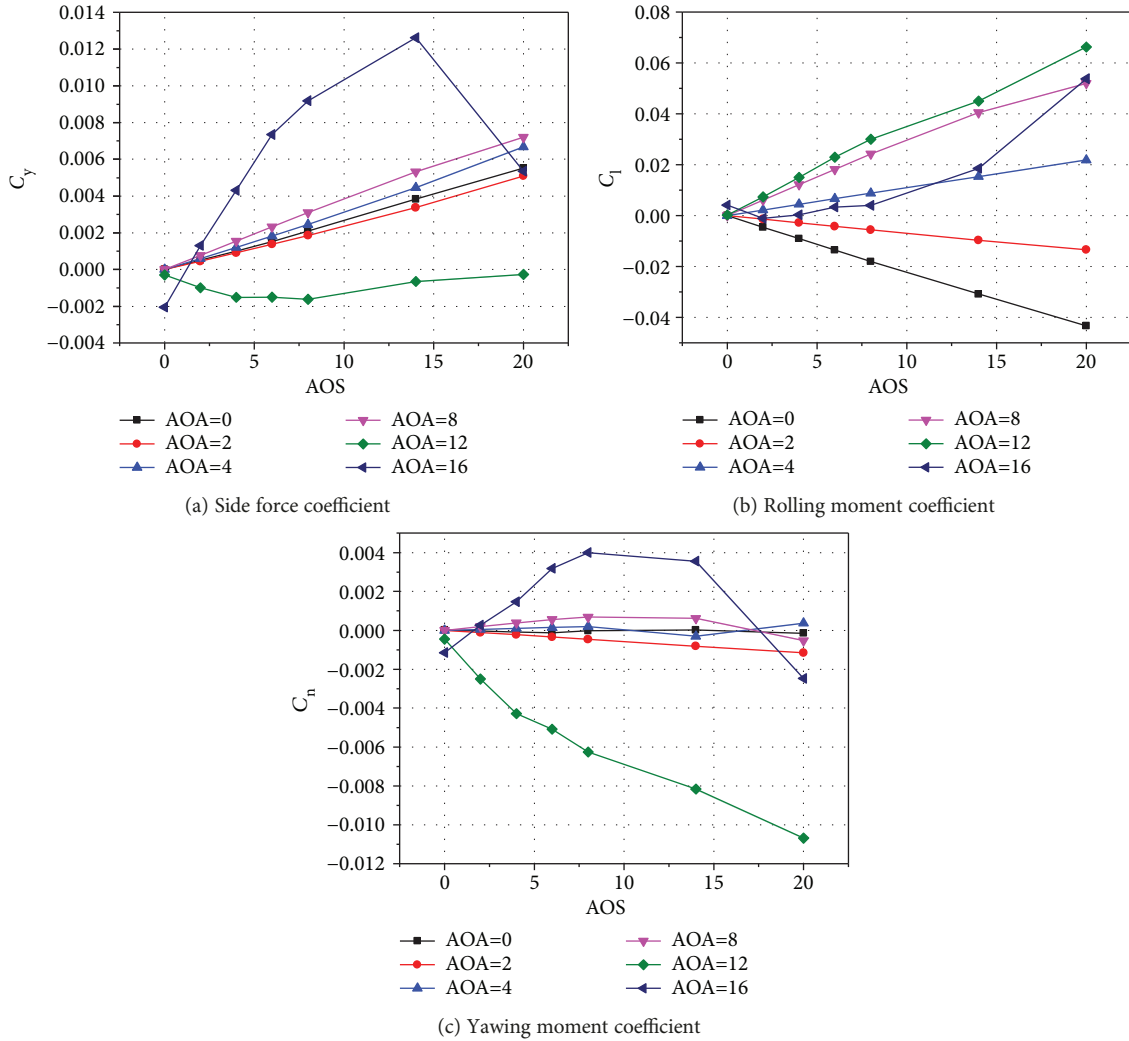


FIGURE 10: Side force, rolling moment, and yawing moment coefficients for the side slip angle.

20° sideslip angle. Flow features are denoted as IS (incipient separation), PS (primary separation), PA (primary attachment), SS (secondary separation), and SA (secondary attachment) in Figure 12(c).

Frink et al. [20] defined the region of incipient separation where the boundary layer vorticity begins organizing into a feeding sheet that eventually leaves the surface to form a primary off-body vortex using the set of dividing streamtraces shown in Figure 12(c). Frink et al. [20] stated that the beginning point of the incipient separation is that where the force balance between streamwise inertia and the spanwise pressure gradient is tipped. In the present work, we clearly identified this region of incipient separation where the skin friction lines downstream of the beginning point were contained outboard of dividing streamtraces and finally returned to the leading edge. Other skin friction lines upstream of this were still attached to flow and exited at the trailing edge. This incipient separation region moved to the apex with an increase in the angle of attack from 12° to 16° as in Figures 8(c) and 12(c). This result is related to movement of the leading edge vortex to the apex. The

secondary separation lines and primary attachment lines also moved to the inboard as the angle of attack increased. However, the inner vortex, which we inferred from the converging skin friction line, formed at the inflection point of the lambda wing without movement as the angle of attack increased. On the windward wing, the separation region of the outboard increased from the trailing edge to the leading edge and to the inboard as the angle of attack increased. This expansion resulted in a decrease in the leading edge vortex on the left wing.

In Figure 14, the vorticity contours in the streamwise direction at 8 yz planes and the streamline around the vehicle are plotted at the sideslip angle, 8°. The angles of attack are corresponding to 8°, 12°, and 14° where the behavior of the side force and yawing moment are shown highly nonlinear. Two coefficients are almost constant at less than the 8° angle of attack but abruptly decrease at 12° and then are recovered to the value before the 8° angle of attack. The vorticity contours and streamline at two angles of attack, 8° and 14°, looks symmetric around the wing tip with respect to the leeward and windward side of the vehicle. Even though a slightly

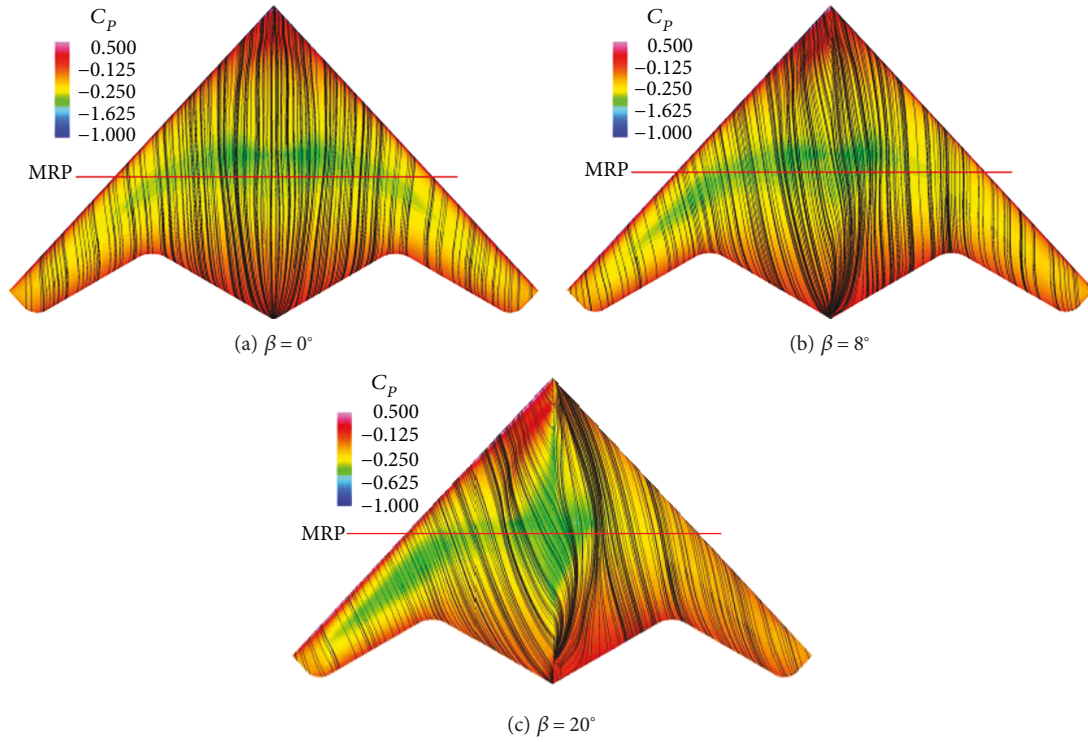


FIGURE 11: Skin friction lines and pressure coefficient contours at angle of attack  $0^\circ$ .

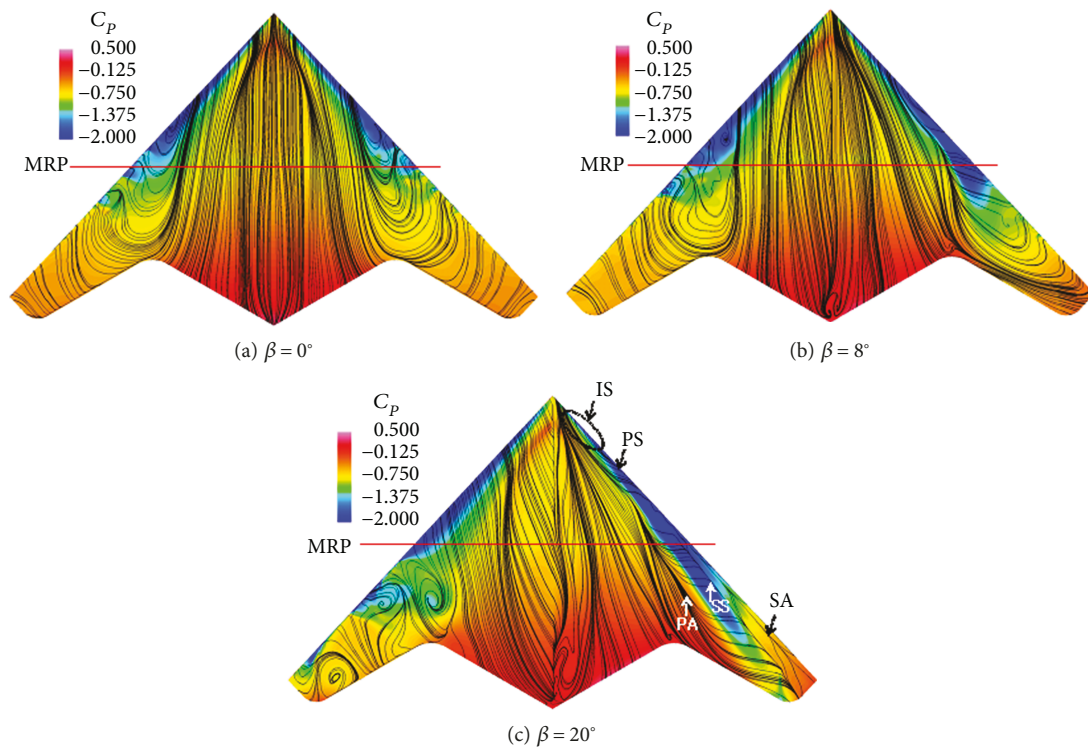


FIGURE 12: Skin friction lines and pressure coefficient contours at angle of attack  $16^\circ$ .

different pattern of streamline between the leeward and windward sides is shown at the angle of attack  $14^\circ$ , the leading edge vortex has been generated in both parts. However, in

the condition of the angle of attack of  $12^\circ$ , this leading edge vortex is shown only in the leeward side. This asymmetric flow structures seem to cause a highly nonlinear behavior

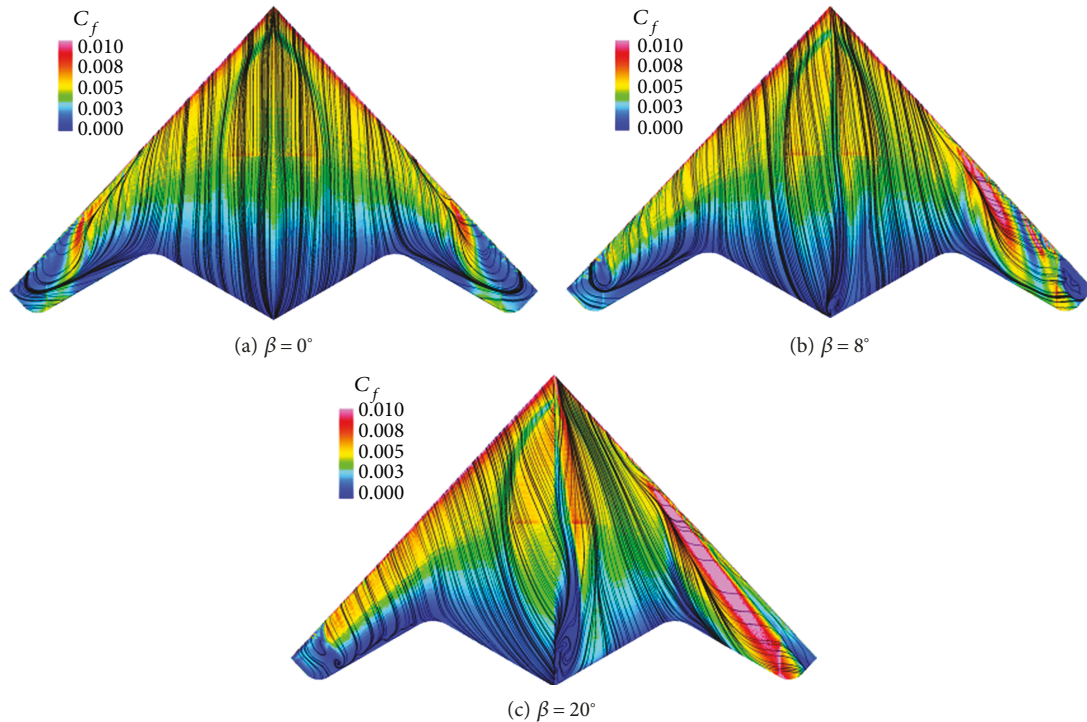


FIGURE 13: Skin friction lines and skin friction contours at angle of attack  $12^\circ$ .

of the side force and yawing moment coefficients. When the streamlines in the leeside at two angles of attack,  $12^\circ$  and  $14^\circ$ , are compared, the different flow patterns can be observed. At the angle of attack of  $12^\circ$ , the tip vortex and the thickness vortex are separated distinctly. However, these two vortices are combined to a large vortex at the angle of attack of  $14^\circ$ . This phenomenon agrees well with the observation of Huber et al. [25] which shows that the rapid increase of the pitching moment occurs at this angle of attack.

Figure 15 shows that the streamlines started from the leading edge, as well as the streamwise vorticity contour at eight different  $yz$  planes at a  $20^\circ$  sideslip angle and a  $16^\circ$  angle of attack. We identified the incipient separation and subsequent vortex formation from the off-body flow structures using streamlines. Even though the secondary vortex cannot be recognized due to screening by the front streamlines, the primary leading edge vortex and inner wing vortex can be seen on the left side. An extra inner wing vortex near the wing root was generated near the apex of the wing on the opposite side. These primary vortex and inner wing vortex structures were confirmed from the streamwise vorticity contours in Figure 15(b). The primary vortex had the highest magnitude vorticity, and the inner vortex had the same sign as the primary one, but it was weaker. The secondary vortex had a distinctly negative streamwise vorticity below the primary vortex. Recent studies of AVT-183 estimated that the inner vortex has its origin near the emergence of the blunt leading edge vortex from the incipient leading edge separation region (refer to Figure 15 in ref. [20]). The present results also show that the origin of the inner vortex is near the incipient separation region of the primary leading edge

vortex. However, these two origins do not overlap as in previous work [20]. There is an attached boundary layer from the leading edge on the upstream half of the opposite wing, while the boundary layers are intricately separated on the downstream half. This pattern can be seen in the skin friction lines of the left wing in Figure 12(c).

#### 4. Conclusions

Here we reported simulation results for the non-slender BWB-type planform with variation in angle of attack ( $-4^\circ$ - $16^\circ$ ) and sideslip angle ( $0^\circ$ - $20^\circ$ ). We analyzed aerodynamic force and moment coefficients as well as flow structures over the upper surface based on the flow mechanism around the delta wing. The side force coefficients and rolling/yawing moment coefficients showed a highly nonlinear behavior with respect to the sideslip angle while the lift and drag force coefficients changed very little with respect to the sideslip angle. As the sideslip angle increased, the pitch break, which is related to the pitching moment coefficient, was delayed up to an angle of attack of  $12^\circ$  compared to  $8^\circ$  at the zero sideslip angle, and the magnitude of increase in pitching moment decreased thereafter. The rolling moment coefficient increased until an angle of attack of  $10^\circ$  or  $12^\circ$  and then decreased thereafter. Among the three moment coefficients, the yawing moment coefficient showed the highest nonlinear behavior as the sideslip angle varied. We plotted the side force and rolling/yawing moment coefficients with respect to the sideslip angle for detailed analysis of the sideslip angle effect. At a small angle of attack, the side force and two moment coefficients showed a linear behavior

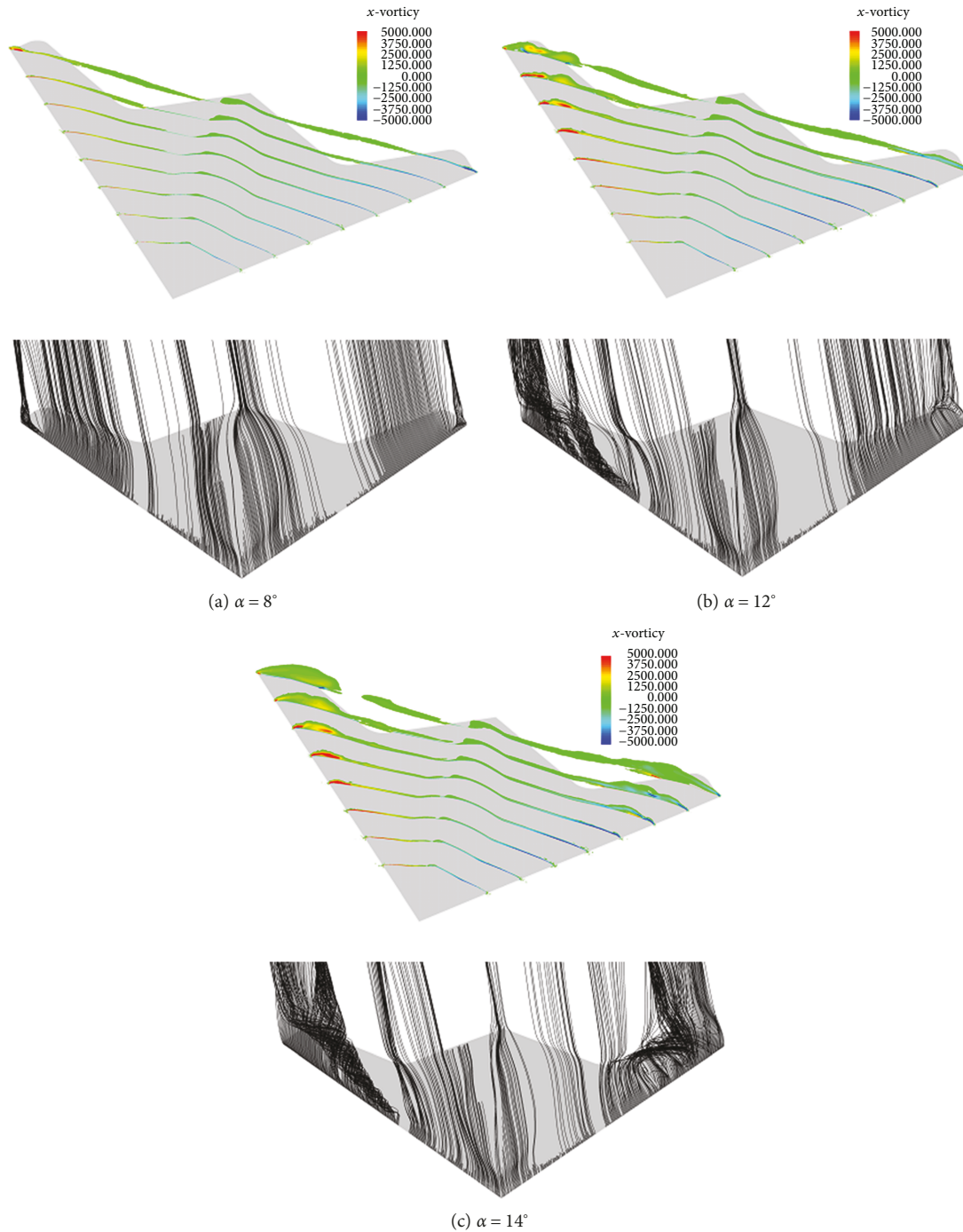


FIGURE 14: Streamwise vorticity contours (upper) and streamlines (lower) at the side slip angle  $8^\circ$ .

with respect to magnitude and rate of change in the angles. However, we observed highly nonlinear behaviors at large angles of attack. At angles of attack of  $12^\circ$  or  $16^\circ$  in the present model, the side force and yawing moment coefficients had values with opposite signs or slopes when compared with results at smaller angles of attack. We confirmed that the present aerodynamic coefficient results are similar to Loefer's experimental results [14].

We interpreted the nonlinear behaviors of aerodynamic coefficients through analysis of the contours of pressure

and skin friction coefficients. Movement to the apex of the leading edge vortex caused the planform to have pitch break with an abrupt increase in the pitching moment. Different decreasing rates of suction pressure at the leading edge of the wings on the windward and leeward sides gave rise to nonlinear changes in the rolling moment. The yawing moment demonstrated the opposite tendency at an angle of attack of  $12^\circ$  due to movement of the primary vortex with high skin friction to the inboard. We also identified the five flow types, which are well known in blunt leading edge swept

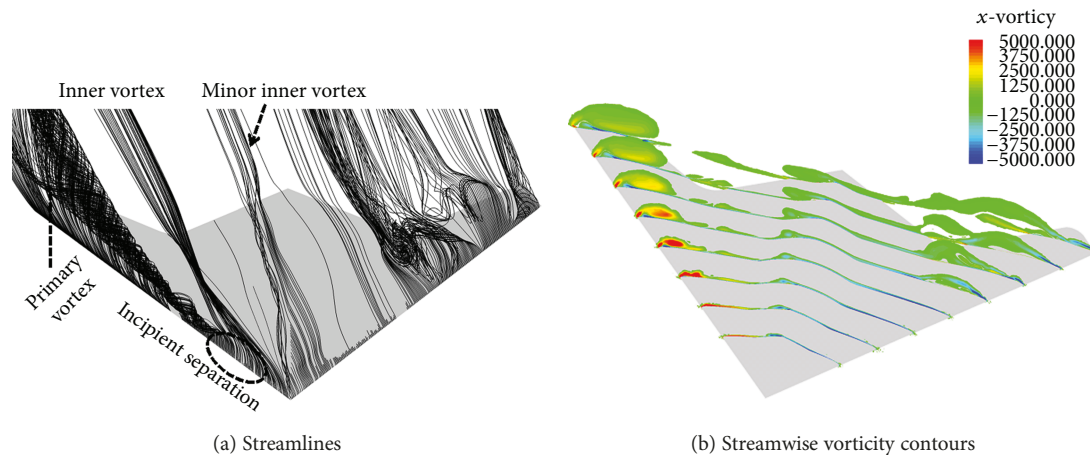


FIGURE 15: Streamlines and streamwise vorticity contours at  $\alpha = 16^\circ$  and  $\beta = 20^\circ$ .

wings, by the skin friction lines and off-body streamlines at large angles of attack and sideslip angles, in particular  $16^\circ$  and  $20^\circ$ , respectively, while we observed only primary attachment and separation by the primary vortex at most angles.

### Data Availability

The data used to support the findings of this study are available from the corresponding author upon request.

### Conflicts of Interest

The authors declare that they have no conflicts of interest.

### Acknowledgments

This research was supported by the Agency for Defense Development (UD170056JD).

### References

- [1] D. John and J. R. Anderson, *Fundamentals of Aerodynamics*, McGraw-Hill, 5th edition, 2010.
- [2] I. Gursul, R. Gordnier, and M. Visbal, "Unsteady aerodynamics of nonslender delta wings," *Progress in Aerospace Science*, vol. 41, no. 7, pp. 515–557, 2005.
- [3] J. M. Luckring and O. J. Boelens, *A Unit-Problem Investigation of Blunt Leading-Edge Separation Motivated by AVT-161 SACCON Research*, NASA Technical Report, 2011.
- [4] S. C. Mcparlin, R. J. Bruce, A. G. Hepworth, and A. J. Rae, "Low speed wind tunnel on the 1303 UCAV concept," in *24th AIAA Applied Aerodynamics Conference, Fluid Dynamics and Co-located Conferences*, San Francisco, CA, USA, June 2006.
- [5] A. Schütte, D. Hummel, and S. M. Hitzel, "Numerical and experimental analyses of the vortical flow around the SACCON configuration," in *28th AIAA Applied Aerodynamics Conference, Fluid Dynamics and Co-located Conferences*, Chicago, IL, USA, June-July 2010.
- [6] T. D. Loeser, D. D. Vicroy, and A. Schutte, "SACCON static wind tunnel tests at DNW-NWB and 14'x22' NASA LaRC," in *28th AIAA Applied Aerodynamics Conference, Fluid Dynamics and Co-located Conferences*, Chicago, IL, USA, June-July 2010.
- [7] J. Lee, B. Lee, M. Kim, and C. Kim, "Active flow control on a UCAV planform using synthetic jets," *International Journal of Aeronautical and Space Sciences*, vol. 17, no. 3, pp. 315–323, 2016.
- [8] M. E. Milne and M. T. Arthur, "Evaluation of bespoke and commercial CFD methods for a UCAV configuration," in *24th AIAA Applied Aerodynamics Conference, Fluid Dynamics and Co-located Conferences*, San Francisco, CA, USA, June 2006.
- [9] D. Vallespin, A. Da Ronch, K. J. Badcock, and O. Boelens, "Vortical flow prediction validation for an unmanned combat air vehicle model," *Journal of Aircraft*, vol. 48, no. 6, pp. 1948–1959, 2011.
- [10] C. David, C. Sukumar, and G. Uri, "Flow prediction around the SACCON configuration using CFD++," in *28th AIAA Applied Aerodynamics Conference, Fluid Dynamics and Co-located Conferences*, Chicago, IL, USA, June-July 2010.
- [11] Y.-H. Jo, K. Chang, D.-J. Sheen, and S. H. Park, "Numerical simulation of aerodynamic characteristics of a BWB UCAV configuration with transition models," *International Journal of Aeronautical and Space Sciences*, vol. 16, no. 1, pp. 8–18, 2015.
- [12] A. Schütte, D. Hummel, and S. M. Hitzel, "Numerical and experimental analyses of the vertical flow around the SACCON configuration," in *28th AIAA Applied Aerodynamics Conference, Fluid Dynamics and Co-located Conferences*, Chicago, IL, USA, June-July 2010.
- [13] P. Kristian, "Low-speed aerodynamic and flowfield characteristics of a UCAV," in *24th AIAA Applied Aerodynamics Conference, Fluid Dynamics and Co-located Conferences*, San Francisco, CA, USA, June 2006.
- [14] T. D. Loeser, D. D. Vicroy, and A. Schütte, "SACCON static wind tunnel test a DNW-NWB and 14'x22' NASA LaRC," in *28th AIAA Applied Aerodynamics Conference, Fluid Dynamics and Co-located Conferences*, Chicago, IL, USA, June-July 2010.
- [15] H. Shim, S. Park, and S. Oh, "An experiment study on sideslip angle effect of lambda wing configuration," *Journal of The Korean Society for Aeronautical and Space Sciences*, vol. 43, no. 3, pp. 224–231, 2015.
- [16] N. T. Frink, "Stability and control CFD investigation of a generic 53-deg swept UCAV configuration," in *32nd AIAA Dynamics and Co-located Conferences*, Chicago, IL, USA, June-July 2010.

*Applied Aerodynamics Conference, AIAA AVIATION Forum, (AIAA 2014-2133)*, Atlanta, GA, USA, 2014.

- [17] M. Ghoreyshi and R. M. Cummings, "Unsteady aerodynamics modeling for aircraft maneuvers: a new approach using time-dependent surrogate modeling," *Aerospace Science and Technology*, vol. 39, pp. 222–242, 2014.
- [18] S. Pfnür and C. Breitsamter, "Unsteady aerodynamics of a diamond wing configuration," *CEAS Aeronautical Journal*, vol. 9, no. 1, pp. 93–112, 2018.
- [19] S. Yayla, C. Canpolat, B. Sahin, and H. Akilli, "Yaw angle effect on flow structure over the nonslender diamond wing," *AIAA Journal*, vol. 48, no. 10, pp. 2457–2461, 2010.
- [20] N. T. Frink, M. Tomac, and A. Rizzi, "Collaborative study of incipient separation on 53°-swept diamond wing," *Aerospace Science and Technology*, vol. 57, pp. 76–89, 2016.
- [21] S. Deck and J. M. Luckring, "Zonal detached eddy simulation (ZDES) of the flow around the AVT-183 diamond wing configuration," *Aerospace Science and Technology*, vol. 57, pp. 43–51, 2016.
- [22] H. Shim and S. Park, "An experimental study on wake characteristics of vane-type vortex generator and its application," Ph D. Thesis, KAIST, 2015.
- [23] ANSYS Inc., *User Manual*, ANSYS ICEM CFD Release 17.0, 2017.
- [24] S. H. Park, K. Chang, H. J. Shim, D. J. Sheen, and S. H. Park, "Computational fluid dynamics of the low-speed longitudinal aerodynamic characteristics for BWB type UCAV configuration," *Journal of Computational Fluids Engineering*, vol. 21, no. 3, pp. 48–54, 2016.
- [25] K. Huber, A. Schutte, and M. Rein, "Numerical investigation of the aerodynamic properties of a flying wing configuration," in *30th AIAA Applied Aerodynamics Conference, Fluid Dynamics and Co-located Conferences*, New Orleans, LA, USA, June 2012.

